Spin-orbit interactions in inversion-asymmetric 2D hole systems: a variational analysis

E. Marcellina,[1] A. R. Hamilton,[1] R. Winkler,[2,3] and Dimitrie Culcer[1]

[1] *School of Physics, The University of New South Wales, Sydney, Australia*
[2] *Deparment of Physics, Northern Illinois University, DeKalb, IL 60115, USA*
[3] *Materials Science Division, Argonne National Laboratory, Argonne, IL 60439, USA*

(Dated: November 2, 2018)

We present an in-depth study of the spin-orbit (SO) interactions occurring in inversion-asymmetric two-dimensional hole gases at semiconductor heterointerfaces. We focus on common semiconductors such as GaAs, InAs, InSb, Ge, and Si. We develop a semi-analytical variational method to quantify SO interactions, accounting for both structure inversion asymmetry (SIA) and bulk inversion asymmetry (BIA). Under certain circumstances, using the Schrieffer-Wolff (SW) transformation, the dispersion of the ground state heavy hole subbands can be written as $E(k) = Ak^2 - Bk^4 \pm Ck^3$ where A, B, and C are material- and structure-dependent coefficients. We provide a simple method of calculating the parameters A, B, and C, yet demonstrate that the simple SW approximation leading to a SIA (Rashba) spin splitting $\propto k^3$ frequently breaks down. We determine the parameter regimes at which this happens for the materials above and discuss a convenient semi-analytical method to obtain the correct spin splitting, effective masses, Fermi level, and subband occupancy, together with their dependence on the charge density, dopant type, and dopant concentration for both inversion and accumulation layers. Our results are in good agreement with fully numerical calculations as well as with experimental findings. They suggest that a naive application of the simple cubic Rashba model is of limited use in common heterostructures, as well as quantum dots. Finally, we find that for the single heterojunctions studied here the magnitudes of BIA terms are always much smaller than those of SIA terms.

I. INTRODUCTION

The ability to harness the spin degree of freedom is essential for the development of practical semiconductor spintronic devices[1,2] and quantum information processing.[3–5] All-electrical spin control may be possible by exploiting the coupling of the spin and orbital degrees of freedom brought about by the strong spin-orbit interactions in certain semiconductor systems.[1,2,6] This could lead to faster spin rotations and lower power consumption, as well as the convenience of using solely electric fields, which are easier to apply and localize than magnetic fields. The search for semiconductor systems with strong spin-orbit coupling has led naturally to low-dimensional hole systems.[7–9] Despite the promising advances of recent years, in particular in the experimental state of the art,[10–22] functional hole spin-based devices have yet to be realized. In particular, a comprehensive understanding of the interaction between a hole's spin and its solid-state environment is far from complete.

In group IV and III-V semiconductors the uppermost valence band is described by wave functions originating from atomic p orbitals with orbital angular momentum $L = 1$. Together with the spin $S = 1/2$ this results in an effective spin $J = 3/2$,[6,23,24] which brings about spin properties of hole systems that are distinct from those of electron systems.[25,26] The valence band eigenstates are heavy holes (HH) with angular momentum projection in the direction of the wave vector $m_J = \pm 3/2$ and light holes (LH) with $m_J = \pm 1/2$. These are degenerate at the zone center but split by a finite energy at nonzero wave vectors. Confinement to the interface of a heterojunction fixes the hole spin quantization axis in the growth direction $\hat{\boldsymbol{z}}$, which here we take to be parallel to (001), and lifts the degeneracy of the HH and LH states at the subband edge (in-plane wave vector $\boldsymbol{k} = 0$). At this point the eigenstates remain pure HH and LH, while at finite $\boldsymbol{k}$, the $\boldsymbol{k}\cdot\boldsymbol{p}$ interaction causes the HH and LH states to mix. However, for typical samples, the $\boldsymbol{k} \neq 0$ subband states can still be regarded as approximately HH- or LH-like.[27]

Inversion asymmetry further lifts the spin degeneracies of HH and LH states at finite wave vector,[6] resulting in additional $\boldsymbol{k}$-dependent energy level splittings. Inversion asymmetry in semiconductor heterostructures may stem from the asymmetry of the confining potential [structural inversion asymmetry (SIA) or Rashba terms[28]] or from the asymmetry of the underlying crystal structure [bulk inversion asymmetry (BIA) or Dresselhaus terms[29]]. BIA and SIA spin splittings are proportional to odd powers of k, with k-linear and k^3 terms frequently representing the dominant contributions. They result in a high degree of non-parabolicity of the hole energy bands. Accounting for the complex couplings between the hole bands is vital if one is to capture all aspects of hole spin dynamics correctly. So far, studies of two-dimensional hole gases (2DHGs) in group IV and III-V structures have been predominantly numerical and always material-specific.[30–37] Calculations for inversion-asymmetric structures are more complex due to the nature of the confining potential. Unlike quantum wells, where the potential shape is approximately fixed, the shape of the confining potential in single heterojunctions is highly density-dependent, thus requiring self-consistent wave functions that produce the potential for a given density.

In this paper, we develop a variational method that en-

ables us to gain a transparent insight into spin-orbit interactions in 2DHGs in III-V and Si-based heterojunctions. We use the Luttinger Hamiltonian[24,38] and the standard envelope function approximation,[6] combined with a simple self-consistent variational approach[39–41] to calculate the spin splitting and effective masses for semiconductors with diamond and zincblende lattices. The variational approach allows one to easily solve for the confinement potential $V(z)$. Once the Luttinger Hamiltonian for the 2DHG is constructed, one can use a Schrieffer-Wolff (SW) transformation[42] (in the context of semiconductors also known as Löwdin perturbation theory[43]) to derive simple analytical expressions for the spin-dependent dispersion of 2D hole systems, which subsequently yields the Fermi level, spin splitting, effective masses and subband occupancy. We apply this method to common semiconductors such as GaAs, InAs, InSb, Ge, and Si, and compare inversion and accumulation layers. Effects of surface termination, which can affect the HH spin splitting,[44] are beyond the scope of this work. These effects are less important for heterojunctions, where the wave functions vanish near the interface.

In the absence of BIA terms, the SW transformation enables one to write the dispersion relation in a rather simple form $E_\pm(k) = Ak^2 - Bk^4 \pm Ck^3$ where A, B, and C are material- and structure-dependent coefficients, and the Ck^3 term represents the Rashba spin splitting.[4,6,7,27,36,45–49] However, the validity of this model is limited to a relatively narrow range of parameters, indicating that in general the HH spin splitting contains additional terms, which are frequently sizeable. The limited applicability of the simple dispersion relation to realistic heterostructures is relevant to the current understanding of the spin-Hall conductivity,[45–47,50] hole spin helix,[48] and *Zitterbewegung*,[49] all of which have been derived based on the assumption that the HH spin splitting is proportional to k^3. Our work can be used to determine spin densities and spin-Hall currents in the same way as for electrons.[51,52] It is also highly relevant to the burgeoning field of hole quantum dots, which are actively researched at present with a view to applications in quantum computing, in particular via electric dipole spin resonance (EDSR).[53] The areal number densities of existing single-hole quantum dots are contained in the parameter ranges we study in this work in 2DHGs.

Apart from fully numerical calculations, two approaches can be adopted in regimes in which the cubic spin splitting approximation is inadequate: one can evaluate higher-order terms in perturbation theory, which quickly becomes cumbersome and intractable, or one can perform a numerical diagonalization of the effective Luttinger Hamiltonian restricted to limited subspace spanned by, e.g., the first and second subbands. In this work, we rely on the latter approach when the perturbative methods fail. Our methods yield an excellent agreement with fully numerical results for GaAs holes.[30,41,54]

This paper is structured as follows: In Sec. II, we review variational methods for 2DHGs in quasi-triangular wells. We then use our methods to calculate the spin splitting and effective masses for 2DHGs based on various materials in Sec. III. The effects of the Dresselhaus SO interaction are outlined in Sec. IV. We discuss our results in Sec. V and summarize our findings in Sec. VI.

TABLE I. Luttinger parameters and bulk Dresselhaus coefficients[6] used in this work, where B_D is in eVÅ^3 and C_D in eVÅ.

	γ_1	γ_2	γ_3	B_D	C_D
GaAs	6.85	2.10	2.90	−81.93	−0.0034
InAs	20.40	8.30	9.10	−50.18	−0.0112
InSb	37.10	16.50	17.70	−934.8	−0.0082
Ge	13.38	4.24	5.69		
Si	4.28	0.34	1.45		

II. THEORETICAL FORMALISM

A. Luttinger Hamiltonian for 2DHGs

We start from the bulk Luttinger Hamiltonian[24,38] describing the effective spin $J = \frac{3}{2}$ valence band holes

$$H_L = \begin{pmatrix} P+Q & 0 & L & M \\ 0 & P+Q & M^* & -L^* \\ L^* & M & P-Q & 0 \\ M^* & -L & 0 & P-Q \end{pmatrix} \tag{1}$$

where

$$P = \frac{\mu}{2}\gamma_1 k^2, \qquad Q = -\frac{\mu}{2}\gamma_2\left(2k_z^2 - k^2\right), \tag{2a}$$

$$L = -\sqrt{3}\mu\,\gamma_3 k_- k_z, \quad M = -\frac{\sqrt{3}\,\mu}{4}\left(\bar{\gamma}^2 k_-^2 + \delta^2 k_+^2\right), \tag{2b}$$

$$\bar{\gamma} = \tfrac{1}{2}\left(\gamma_2 + \gamma_3\right), \qquad \delta = \tfrac{1}{2}\left(\gamma_2 - \gamma_3\right), \tag{2c}$$

$$k^2 = k_x^2 + k_y^2, \qquad k_\pm = k_x \pm i k_y, \tag{2d}$$

$\mu \equiv \hbar^2/m_0$ with bare electron mass m_0, and γ_1, γ_2, and γ_3 are the Luttinger parameters, see Table I. The wave vector components are defined by the crystallographic orientation. In this work, we consider holes grown on a (001) surface so that $k_x \parallel (100)$, $k_y \parallel (010)$, and $k_z \parallel (001)$.

We have expressed H_L in the basis of J_z eigenstates $\{|+\frac{3}{2}\rangle, |-\frac{3}{2}\rangle, |+\frac{1}{2}\rangle, |-\frac{1}{2}\rangle\}$. The Luttinger Hamiltonian is further simplified in the axial approximation, where the terms proportional to δ are neglected.[6,30] The axial approximation is appropriate for GaAs, InAs, InSb and Ge, while for Si δ is significant (Table I) and we expect a highly anisotropic Fermi contour, as Sec. III C will show.

The 4×4 Luttinger Hamiltonian (1) is accurate as long as the spin-orbit split-off band is far away from the HH and LH bands. The energy gap Δ_{SO} separating the split-off band from the HH-LH manifold is of the order

of $300-800$ meV for GaAs, InAs, InSb, and Ge.[6] For Si, $\Delta_{\rm SO}=44$ meV, and thus the couplings to the split-off band must be taken into account.

B. Poisson and Schrödinger Equations

We consider a single heterojunction with the interface at $z=0$. We assume that the wave functions vanish at the interface so that in the following we restrict ourselves to $z\geq 0$. Our calculation is based on two steps, each of which is variational in nature. First we construct the self-consistent potential $V(z)$ characterizing the heterojunction neglecting the subtleties in the dispersion of the 2DHG. Then we solve H_L for $V(z)$ in a second variational calculation.

The one-dimensional charge distribution giving rise to the confinement potential $V(z)$, consists of two contributions: the 2D hole density $p|\psi_h(z)|^2$, and the net dopant impurity concentration $N_{\rm imp}$. The corresponding Poisson equation is thus:

$$\frac{d^2}{dz^2}V(z)=-\frac{e^2}{\epsilon_s\epsilon_0}\left[p|\psi_h(z)|^2+N_{\rm imp}\right], \tag{3}$$

where ϵ_s is the dielectric constant of the semiconductor, ϵ_0 is the vacuum permittivity, p denotes the number density of 2D holes, and $\psi_h(z)$ is the zero-node HH wave function, assuming the most common case that only the lowest subband labelled HH1 is occupied. For $V(z)$ we neglect k-dependent band mixing, which has only a small effect on $V(z)$. We approximate the wave function using the Fang-Howard variational scheme, which takes the form[39]

$$\psi_v(z)=2\lambda_v^{3/2}z\exp(-\lambda_v z) \tag{4}$$

where $v=h$ represents the zero-node HH1 wave function. The solution of the Poisson equation (3), in the Hartree approximation,[55,56] is given by:

$$V(z)=V_{\rm 2DHG}(z)+V_{\rm imp}(z) \tag{5}$$

where $V_{\rm 2DHG}(z)$ is the electrostatic potential due to the ground state heavy holes and $V_{\rm imp}(z)$ is due to the depletion layer dopant impurities.[30,56] The term $V_{\rm 2DHG}(z)$, obtained using the Fang-Howard wave function (4), reads

$$V_{\rm 2DHG}(z)=\frac{pe^2}{\epsilon_s\epsilon_0}\left[z-\int_0^z dz'\int_0^{z'}dz''|\psi_h(z'')|^2\right] \tag{6a}$$

$$=\frac{pe^2}{\epsilon_s\epsilon_0}\left[e^{-2z\lambda_h}\left(2z+\frac{3}{2\lambda_h}+z^2\lambda_h\right)-\frac{3}{2\lambda_h}\right], \tag{6b}$$

whereas the impurity contribution reads

$$V_{\rm imp}(z)=\frac{e^2}{\epsilon_s\epsilon_0}N_{\rm imp}\left(w_{\rm depl}z-z^2/2\right), \tag{7}$$

where

$$w_{\rm depl}\equiv\sqrt{\frac{2\epsilon_s\epsilon_0}{e^2N_{\rm imp}}\left[\Phi+E_{H1}+E_{F1}-\frac{e^2}{\epsilon_s\epsilon_0}p\langle z\rangle\right]} \tag{8}$$

is the depletion width that depends on the dopant concentration, ground state HH energy E_{H1}, Fermi energy $E_{F1}\equiv E_F-E_{H1}$, and band bending Φ.[56]

The wave function $\psi_h(z)$ entering the Poisson equation (3) is the solution of the Schrödinger equation. Thus one usually solves the Poisson and Schrödinger equations self-consistently.[30,31,33,35,36,57] Using $V(z)$ from the Poisson equation, the 2D hole density $p|\psi_h(z)|^2$ is obtained from the Hamiltonian, from which one then constructs a new $V(z)$ by solving the Poisson equation. The process is iterated until $V(z)$ converges. In this work, we instead employ a simplified procedure based on the self-consistent variational scheme in Ref. 41, which yields good agreement with fully self-consistent numerical calculations. Here the variational parameter λ_h is obtained by minimizing the ground state HH energy E_{H1}, which, neglecting band mixing, is the sum of the diagonal matrix elements of the Luttinger Hamiltonian in Eq. (1) for the HH subspace and $V(z)$ in Eq. (3), taking into account that E_{H1} also appears in Eq. (8).

In a second variational step, we obtain the $\boldsymbol{k}$ and spin dependent eigenfunctions $\Psi_{h\boldsymbol{k}}(z)$ of the total Hamiltonian $\tilde{H}=H_L+V(z)$ for the HH1 subband by expanding $\Psi_{h\boldsymbol{k}}(z)$ in terms of the lowest eigenstates of $\tilde{H}$ for $\boldsymbol{k}=0$, when $\tilde{H}$ becomes diagonal. For the $\boldsymbol{k}=0$ HH1 and LH1 states we use the zero-node wave functions (4) with $v=h,l$. For the one-node HH2, LH2 states we use the form[32,40]

$$\psi_w(z)=\sqrt{12}\lambda_w^{3/2}z\left[1-(\lambda_v+\lambda_w)\,z/3\right] \times \mathrm{e}^{-\lambda_w z}/\sqrt{1-\lambda_v/\lambda_w+\lambda_v^2/\lambda_w^2}, \tag{9}$$

where λ_w with $w=H,L$ denote additional variational parameters. The introduction of these additional variational parameter gives more accurate results[40] than a single variational parameter $\lambda_v{=}\lambda_w$. The eigenvalues $E(\boldsymbol{k})$ and the corresponding $\boldsymbol{k}$ dependent expansion coefficients are obtained by diagonalizing the matrix $\tilde{H}$, whose elements are given as

$$\tilde{H}_{\nu\nu'}=\langle\nu|H_L+V(z)|\nu'\rangle, \tag{10}$$

where $|\nu\rangle$ denotes the wave functions (4) and (9).

C. Schrieffer-Wolff Transformation and Rashba Spin-Splitting

The 8×8 matrix (10) can be diagonalized numerically. To obtain analytical expressions for the dispersion of the HH1 subband, one can apply a Schrieffer-Wolff transformation[42] (Löwdin perturbation theory[43]) to the

TABLE II. Values for material- and structure-dependent coefficients A (in 10^{-16} meV m^2), B (in 10^{-32} meV m^4), and $C \equiv |\alpha_R|$ (in 10^{-24} meV m^3) in the dispersion relation $E(k) = Ak^2 - Bk^4 \pm Ck^3$, the energies E_{H1}, Δ_{11}^{HL}, $E_{F1} \equiv E_F - E_{H1}$ (in meV), and spin splitting for GaAs inversion and accumulation layers with $N_D - N_A = 3 \times 10^{20}$ m^{-3}. The densities are in 10^{15} m^{-2}. For inversion layers, Schrieffer-Wolff fails when the density is $\gtrsim 2.5 \times 10^{15}$ m^{-2}. For accumulation layers, the Schrieffer-Wolff approach is valid up to a density of 5×10^{14} m^{-2}.

Density	A	B	C	E_{H1}	Δ_{11}^{HL}	E_{F1}	Δp[a]	Δp[b]
				Inversion layer				
0.5	3.02	0.28	0.51	16.12	8.32	0.91	0.10	0.14
1.0	3.00	0.27	0.53	19.24	8.73	1.67	0.18	0.23
1.5	2.98	0.25	0.56	22.12	9.04	2.30	0.25	0.30
2.0	2.96	0.24	0.58	24.83	9.27	2.83	0.31	0.35
2.5	2.94	0.24	0.61	27.40	9.46	3.26	0.36	0.39
3.0				29.85	9.62	3.64	0.41	0.42
				Accumulation layer				
0.5	2.90	0.81	1.24	8.84	2.68	0.70	0.31	0.33
1.0				12.85	2.87	1.06	0.48	0.43
1.5				16.30	2.97	1.36	0.55	0.47
2.0				19.42	3.04	1.66	0.58	0.49
2.5				22.31	3.08	1.96	0.60	0.50
3.0				25.02	3.12	2.28	0.60	0.51

[a] Calculated using variational method and a numerical diagonalization of Eq. (10).
[b] Calculated using fully numerical method devised in Refs. 41 and 54.

matrix (10) yielding in lowest order the following effective 2×2 Hamiltonian for the $\{|\pm\frac{3}{2}\rangle\}$ subspace

$$H_{2\times 2} = (Ak^2 - Bk^4)\mathbb{I}_{2\times 2} + \alpha_R(k_+^3\sigma_- - k_-^3\sigma_+), \quad (11)$$

where A and B describe the orbital part of the energy dispersion, and α_R is the Rashba spin-orbit coefficient arising from the inversion asymmetry of $V(z)$. The coefficients A, B, and α_R are evaluated to lowest order in the perturbation expansion, and their expressions are given in the Appendix.

The term $\alpha_R(k_+^3\sigma_- - k_-^3\sigma_+)$ in Eq. (12) gives the Rashba spin splitting which lifts the spin degeneracy at finite k. The corresponding dispersion relation takes the simple form

$$E_\pm(k) = Ak^2 - Bk^4 \pm Ck^3, \quad (12)$$

where $C \equiv |\alpha_R|$. Numerical values for A, B, and $C \equiv |\alpha_R|$ for typical experimental densities are given in Table II. The resulting subbands, denoted as HH1+ and HH1−, have unequal subband populations $p_\pm$ and density of states (DOS) effective masses $m_\pm$.

We use the dimensionless quantity

$$\Delta p \equiv \frac{|p_+ - p_-|}{p} \quad (13)$$

to characterize the strength of the Rashba spin-orbit interaction. Experimentally, the quantity Δp is usually inferred by analyzing the beating pattern of Shubnikov-de-Haas (SdH) oscillations[6,57–60] and can be manipulated by tuning the density p. At low temperature, the spin subband populations become

$$p_\pm = \int \frac{d^2k}{(2\pi)^2}\theta[E_F - E_\pm(k)]. \quad (14)$$

where θ is the Heaviside step function. For hole systems with isotropic Fermi contours, Eq. (14) becomes

$$p_\pm = \frac{k_{F\pm}^2}{4\pi}. \quad (15)$$

Using the coefficients in Eq. (12), this translates to

$$p_\pm = \frac{p}{2} \pm \frac{pc}{\sqrt{2}X}\sqrt{p\pi\left(6 - \frac{4}{X}(1 - 4p\pi b)\right)} \quad (16)$$

where

$$X \equiv 1 - 4p\pi b + \sqrt{1 - 4p\pi(2b + c^2 - 4b^2p\pi)} \quad (17a)$$

$$b \equiv B/A \qquad c \equiv C/A \quad (17b)$$

so that the Rashba spin splitting Δp is given by

$$\Delta p = \frac{\sqrt{2}c}{X}\sqrt{p\pi\left(6 - \frac{4}{X}(1 - 4p\pi b)\right)}. \quad (18)$$

The DOS effective masses $m_\pm$ of the spin-split subbands at the Fermi energy E_F takes the form

$$\frac{m_\pm}{m_0} = \frac{\mu}{2\pi}\int d^2k\delta[E_F - E_\pm(k)]. \quad (19)$$

For isotropic bands, this becomes

$$\frac{m_\pm}{m_0} = \mu\left(\frac{1}{k}\frac{dE_\pm(k)}{dk}\right)^{-1}_{k=k_{F\pm}}, \quad (20a)$$

$$= \frac{\mu}{2A - 4Bk_{F\pm}^2 \pm 3Ck_{F\pm}}. \quad (20b)$$

where the Fermi wave vectors $k_{F\pm}^2$ for a given total density p are evaluated using Eqs. (15) and (16).

D. Comparison with Numerical Results

To illustrate our approach, Fig. 1 shows a comparison between the results obtained using our variational calculation and those obtained using an iterative Fang-Howard and Luttinger Hamiltonian scheme in Ref. 30. The 2DHG considered in Ref. 30 is a hole GaAs single heterojunction with a density of 5×10^{15} m^{-2} and a net dopant concentration of $N_D - N_A = 3 \times 10^{20}$ m^{-3}.[61] The confinement potential $V(z)$ obtained from solving Eq. (3) is shown in the inset of Fig. 1. Our variational approach slightly overestimates the ground state heavy hole energy E_{H1} compared to the numerical results, as expected for a variational calculation. The corresponding DOS effective masses, obtained from Eq. (20), are $m_+ = 0.52\ m_0$ and $m_- = 0.12\ m_0$. These numbers are in close agreement with the full-numerical calculations in Ref. 30, where $m_+ = 0.46\ m_0$ and $m_- = 0.12\ m_0$.

We also find good agreement between our variational results for the Rashba spin splitting Δp and those obtained using the numerical method described in Refs. 41 and 54 (see Table II).

While the simple dispersion in Eq. (12) affords a convenient way to calculate DOS properties such as effective masses and spin splittings, the validity of the Schrieffer-Wolff transformation is limited to certain sets of densities and dopant concentrations. When the separation between subband energies is small, the coefficients A, B and C are overestimated (refer to Appendix to see the dependence of A, B and C on the energy separations) and one can no longer describe the HH1+ and HH1− bands by Eq. (12). For example, using the values in Table II, for a GaAs inversion layer with $p = 2.5 \times 10^{15}$ m^{-2} and $N_D - N_A = 3 \times 10^{20}$ m^{-3}, the Rashba term Ck^3 becomes larger than $Ak^2 - Bk^4$ so that the heavier HH1+ band bends down at $k_{\rm bend} = 1.7 \times 10^8$ m^{-1}. As $k_{F+} = 1.5 \times 10^8$ m^{-1} is very close to HH1+ turning point $k_{\rm bend}$, the HH1+ dispersion is almost flat at k_{F+}, which means that the HH1+ effective mass is overestimated. The Schrieffer-Wolff results for GaAs inversion layers with $N_D - N_A = 3 \times 10^{20}$ m^{-3} and $p \gtrsim 2.5 \times 10^{15}$ m^{-2} are invalid and we resort to a numerical diagonalization of Eq. (10) to obtain the energy dispersion.

III. FULL RASHBA SPIN-SPLITTINGS AND EFFECTIVE MASSES

In all the structures discussed in this paper, at the densities we consider, only the HH1+ and HH1− bands are occupied (Tables II, IV, and V). Generally, spin splittings for holes are much larger than for electrons: for electron inversion layers with the same doping concentration, the spin splittings are two orders of magnitude smaller.[6]

Below we focus first on GaAs inversion and accumulation layers, which are distinguished by the position of the Fermi level E_F in the subtrate: E_F is pinned near the conduction (valence) band in an inversion (accumulation) layer. Finally, we discuss the spin splitting and effective masses in InAs, InSb, Ge, and Si hole inversion layers.

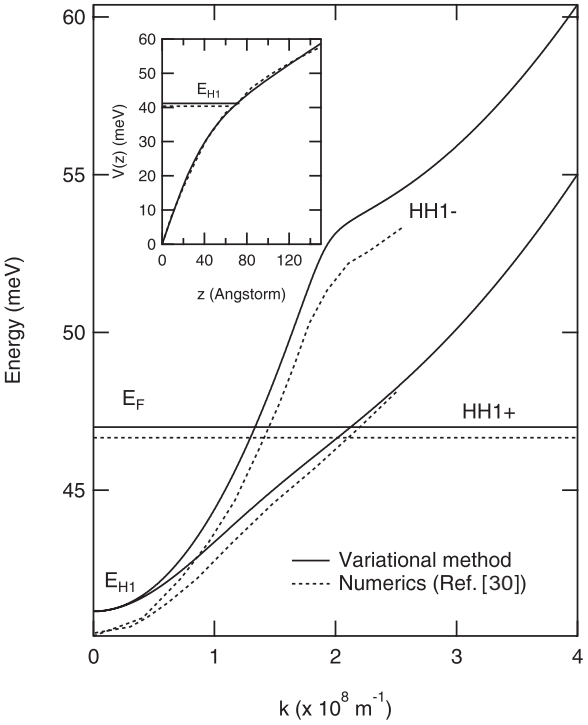

FIG. 1. Comparison between the variational calculations adopted in this work (solid lines) and the numerical calculations in Ref. 30 (dotted lines), showing the inversion-asymmetric potential (inset) and the spin-split HH1+ and HH1− subbands. The system is a GaAs single heterojunction (SHJ) with a 2D hole density of $p = 5 \times 10^{15}$ m^{-2} and a net dopant concentration of $N_D - N_A = 1 \times 10^{21}$ m^{-3}.

A. GaAs Inversion and Accumulation Layers

The type of background dopant determines the location of the Fermi level E_F in the substrate and hence the amount of valence band bending Φ at the heterojunction interface [Fig. 2(a)]. For an accumulation layer, the band bending is less than that of an inversion layer. Thus, in accordance to Gauss' law, for the same density, the confinement potential for an accumulation layer is less steep than in an inversion layer [Fig. 2(b)]. This means that the spacing between subbands is smaller (Fig. 3 and Table II), hence, according to the expressions in the Appendix, the Rashba SO interaction is stronger in an accumulation layer.

The variational approach followed in this work is designed to yield the energies of the HH1± subbands. Although it is not intended to give reliable values for the higher subbands, some qualitative observations can be made concerning the HH1-LH1 spacing in inversion and accumulation layers. In Table II and Fig. 3, the HH1-LH1

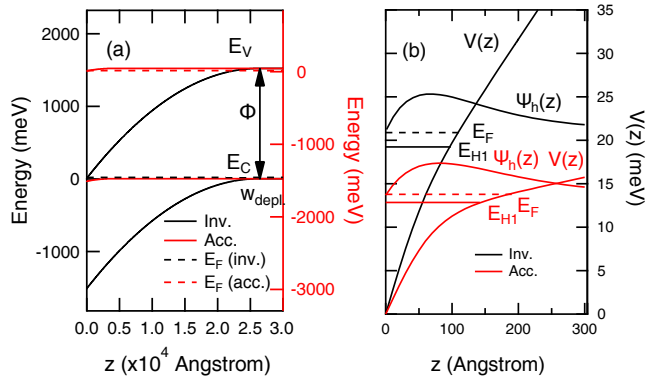

FIG. 2. (Color online) Comparison of the (a) band structure and (b) confinement potential for a GaAs 2D hole system in an inversion and an accumulation layer with a density of 1×10^{15} m^{-2}, where the net dopant concentration is $N_D - N_A = 3 \times 10^{20}$ m^{-3} and $N_D = 3 \times 10^{20}$ m^{-3}, respectively. Due to the magnitude of band bending, the potential for an inversion layer is steeper than that of an accumulation layer.

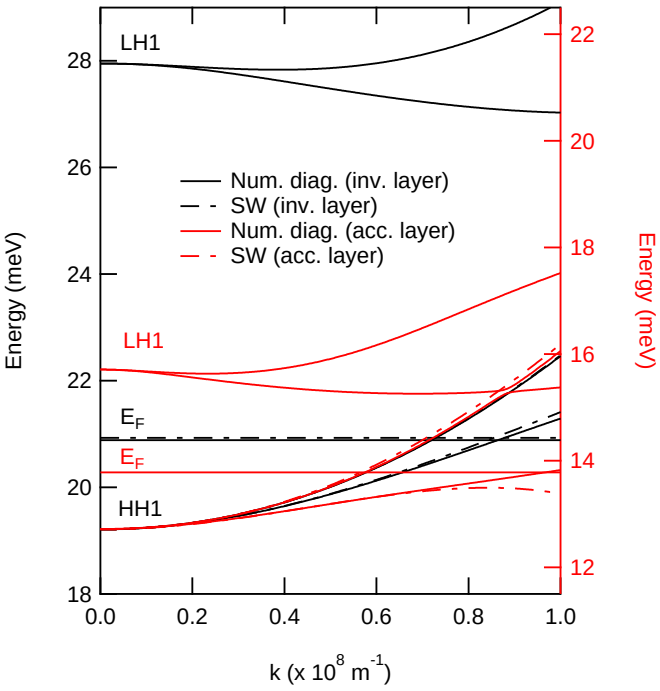

FIG. 3. (Color online) Dispersion for 2D holes in a GaAs inversion (black lines) and a GaAs accumulation layer (red lines) with a density of 1×10^{15} m^{-2}. The doping concentration is $N_D - N_A = 3 \times 10^{20}$ m^{-3} for the inversion layer and $N_D = 3 \times 10^{20}$ m^{-3} for the accumulation layer. The SW dispersion closely matches the numerical diagonalization results (black solid lines) up to k_F for the inversion layer (black dash-dotted lines). In the accumulation layer, the HH1-LH1 separation is closer than in the inversion layer, so that the HH1-LH1 anti-crossing occurs at a lower k compared to the inversion layer and the SW treatment fails at this density (red dash-dotted lines).

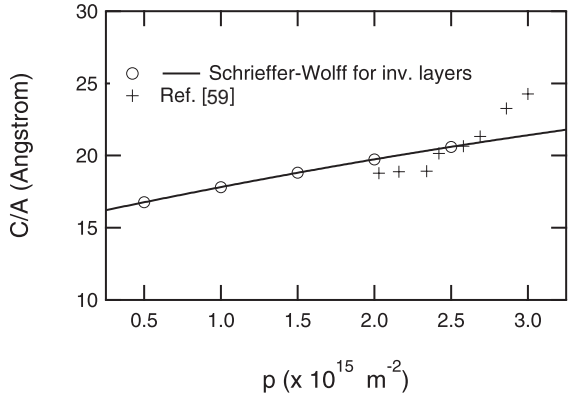

FIG. 4. The ratio of C to A in the dispersion relation of $E(k) = Ak^2 - Bk^4 \pm Ck^3$ for GaAs inversion layers with a dopant concentration of 3×10^{20} m^{-3}. The trend we predict agrees with the experimental results in Ref. 59.

separation $\Delta_{11}^{HL} \equiv |E_{H1} - E_{L1}|$ at $k = 0$ is smaller in an accumulation layer than in an inversion layer at the same density (Table II). Since the Rashba coefficient increases as the subbands get closer together, it is larger in an accumulation than an inversion layer at a given density (see Appendix for the dependence of the Rashba coefficient on the subband energy separations). The Rashba coefficient increases with density, which is consistent with the experimental results in Ref. 59 (Fig. 4).

We compare the different trends in the Rashba spin splitting Δp as a function of density in inversion and accumulation layers in Fig. 5(a) and (b). As expected, the Rashba spin splitting Δp increases with density in both inversion and accumulation layers, consistent with the experimental observations of Ref. 60. However, there is a difference between the dependence of Δp on density for the inversion and accumulation layers. For inversion layers with $N_D - N_A = 3 \times 10^{20}$ m^{-3} and p ranging from 5×10^{14} m^{-2} to 3×10^{15} m^{-2}, the Rashba spin splitting increases with density in an almost linear fashion. In the accumulation layer counterparts, however, the spin splitting increases in an almost linear fashion at lower densities but saturates at higher densities. This feature can be attributed to the fact that, in an accumulation layer, the HH1-LH1 separation is smaller than in an inversion layer such that the HH1− band anti-crosses with the next highest energy subband (LH1) at a lower k than in an inversion layer at the same density (Fig. 3). Consequently, for an accumulation layer with a higher density, k_{F-} can be near the HH1-LH1 anti-crossing. In the anti-crossing region the HH1− band is pushed down in energy, hence the separation between the HH1− and HH1+ bands is reduced.

The strength of the Rashba SOI is also evident in the difference between the HH1+ and HH1− effective masses. Fig. 5(c) and 5(d) show the variation of the effective HH1+ and HH- masses with density. As the figures show, there is a remarkable distinction in the dependence of the m_+ and m_- on density for the in-

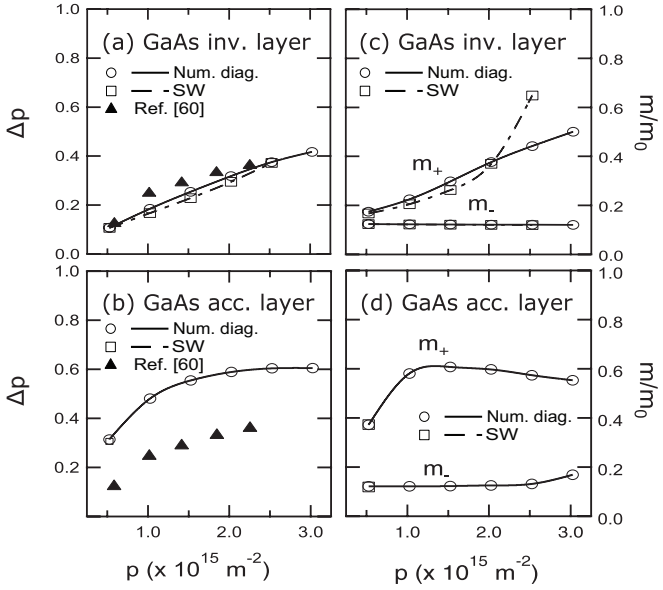

FIG. 5. Rashba spin splitting Δp for holes in (a) GaAs inversion and (b) accumulation layers compared to the experimental results in Ref. 60. The saturation of the spin splitting in accumulation layers is due to the HH1-LH1 anti-crossing. In (c) we show the effective masses $m_\pm$ of GaAs inversion layers and in (d), of accumulation layers. The heavier mass m_+ increases with density whereas m_- is nearly density-independent. In the accumulation layers, m_+ also saturates with density due to the proximity of k_{F-} to the HH1-LH1 anti-crossing. The doping concentration is $N_D - N_A = 3\times10^{20}$ m^{-3} for the inversion layers and $N_D = 3\times10^{20}$ m^{-3} for the accumulation layers.

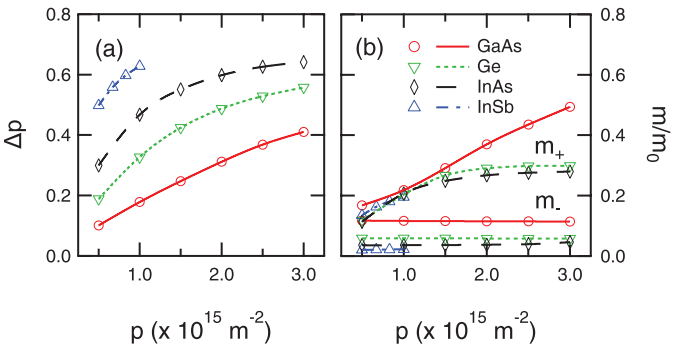

FIG. 6. (Color online) (a) Rashba spin splitting Δp and (b) effective masses $m_\pm$ for various inversion layers. Here, $N_D - N_A = 3\times10^{20}$ m^{-3}. Here, the results are obtained from a numerical diagonalization of Eq. (10).

version and accumulation layers we consider. For the inversion layers studied here, the HH1+ effective mass also increases in an almost linear fashion with density, whereas m_- is essentially constant. The increase in the difference between the effective masses m_+ and m_- with density again implies that the strength of the Rashba SO interactions increase with density. Comparison between numerical and SW results for inversion layers with densities up to $p = 2\times10^{15}$ m^{-2} shows the SW approach works well. However, at density $p = 2.5\times10^{15}$ m^{-2}, the HH1+ effective mass, calculated using the values in Table II, is overestimated [Fig. 5(c)], which signifies that SW breaks down. For the accumulation layers considered here, however, with densities ranging from 5×10^{14} m^{-2} to 3×10^{15} m^{-2}, the HH1+ effective mass increases, then saturates, and becomes increasingly lighter as density increases. The SW approach is only valid for densities up to $\sim 5\times10^{14}$ m^{-2} for the accumulation layers. That SW fails at lower densities in accumulation layers is expected as the separation between subband energies in an accumulation layer is smaller than in an inversion layer at a given density. On the other hand, the HH1− effective mass is essentially constant at lower densities but increases slightly at a higher density of $p = 3\times10^{15}$ m^{-2} [Fig. 5(d)]. The dependence of the HH1+ effective mass m_+ on density can be explained by examining a typical accumulation layer band structure (Fig. 3). As the density increases, the Fermi energy increases, and the fact that the HH1+ band curvature becomes slightly steeper at $k > 1\times10^8$ m^{-1} means that the HH1+ effective mass at the Fermi energy decreases slightly with increasing density. The behavior of HH1−, on the other hand, reflects the anti-crossing between the HH1-LH1 bands. As explained above, at a sufficiently high density, k_{F-} can be very close to the HH1-LH1 anti-crossing. In this region, the HH1− band becomes flatter, hence the corresponding effective mass m_- increases slightly.

B. Zincblende Materials and Ge Inversion Layers

Fig. 6 shows the spin splitting Δp and effective masses $m_\pm$ as functions of density for inversion layers in GaAs, Ge, InSb, and InAs. The strength of the SO interaction is reflected in the difference between the subband populations and effective masses of the HH1+ and HH1− subbands. In Ge, InAs, and InSb, the Rashba spin splitting and HH1+ effective mass m_+ saturate at a lower density compared to GaAs. The saturation of the spin splitting and m_+ indicates that HH1 and LH1 are close enough such that the HH1-LH1 anti-crossing occurs near E_F. This indicates that Ge, InSb, and InAs exhibit a stronger SO interaction than GaAs, which is consistent with the known fact that SO coupling is stronger in compounds containing elements with larger atomic numbers Z. The corollary of this is that SW breaks down at different densities for various materials, which means that Eq. (12) can be valid only for low densities for heavy materials. For example, using the values for A, B, and C listed in Table III, one can get a reasonable estimate for the HH1+ and HH1− effective masses of InAs and Ge at a density of 5×10^{14} m^{-2}. The SW effective masses of InAs are obtained as $m_+ = 0.091\ m_0$ and $m_- = 0.035\ m_0$, which are close to $m_+ = 0.113\ m_0$ and $m_- = 0.036\ m_0$ obtained by numerically diagonalizing Eq. (10). For Ge, the SW effective masses are $m_+ = 0.104\ m_0$ and $m_- = 0.059\ m_0$,

which are in excellent agreement with the numerical diagonalization results $m_+ = 0.118\ m_0$ and $m_- = 0.059\ m_0$.

C. Silicon Inversion Layers

In Si, the hole density is usually in the order of 10^{16} m^{-2}, so that $k_F \sim 5 \times 10^{-8}$ m^{-1}.[62] In this regime, the term Ck^3 in Eq. (12) becomes dominant, SW breaks down and only numerical diagonalization gives reliable results. As pointed out previously, due to the large cubic terms, it is necessary to include the spin-orbit split-off band, hence the Luttinger Hamiltonian is now projected onto a 12×12 subspace. In this work, we consider densities up to 2×10^{16} m^{-2} (Table VI), as for densities higher than these, the higher subband will start to populate, violating our initial assumption.

Due to the significant size the term δ in Eq. (1) the SO interaction and hence spin splitting (14) is anisotropic: it is a minimum along the (100) direction but a maximum along (110). The anisotropy of the SO strength is shown in Fig. 7(a): the difference in the Fermi wave vectors k_{F+} and k_{F-} is 6×10^6 m^{-1} along (100) and 1×10^8 m^{-1} along (110). The equienergy lines for Si ground state HHs [Figs. 7(b) and 7(c)] show that Si valence bands are in general warped, and the warping becomes more pronounced as the density increases.

The spin splitting in Si [Fig. 7(d)] also increases with density, which again, reflects the fact that the strength of spin-orbit interaction increases with density. However, spin splittings in Si holes are smaller than zincblende materials and Ge discussed in the previous section. This is expected since amongst the materials considered in this paper, Si is the lightest element with atomic number $Z = 14$. Nevertheless, the spin splitting in Si holes is still much larger than in Si electrons.

IV. DRESSELHAUS SPIN-ORBIT INTERACTION

In semiconductor crystals which lack a center of inversion, such as GaAs, InAs, and InSb, Dresselhaus spin-orbit interaction terms are present.[29] In this section, we discuss the spin splitting as a function of density and materials (i.e., GaAs, InAs, and InSb) when both Rashba and Dresselhaus interactions are present. We stress that the Dresselhaus interactions are absent in semiconductors with diamond structure such as Si and Ge, although analogous terms of identical symmetry may appear depending on the surface termination.[44] Such terms are not considered explicitly in this work.

The Dresselhaus SO interaction, for bulk holes, is[6,29]

$$\begin{aligned} H_D &= B_D \left[J_x k_x \left(k_y^2 - k_z^2 \right) + \mathrm{cp} \right] \\ &\quad + C_D \left[k_x J_x \left(J_y^2 - J_z^2 \right) + \mathrm{cp} \right] \end{aligned} \tag{21}$$

where B_D is the bulk cubic-k Dresselhaus coefficient, C_D is the bulk linear-k Dresselhaus coefficient (to be distinguished from the coefficient C resulting from the SW transformation), $J_i, i = x, y, z$ are the spin-3/2 matrices, and cp denotes cyclic permutation. The values of B_D and C_D used in this work are given in Table I.

To examine the spin splitting when both Rashba and Dresselhaus terms are present, Eq. (21) is first projected onto the zero- and one-node hole states. Then, by means of the SW transformation, we obtain an effective 2×2 Hamiltonian describing the Dresselhaus interactions in the HH1$\pm$ subspace

$$\begin{aligned} H_{D,2\times2} &= \beta_D \left(\sigma_- k_+ k_- k_+ + \sigma_+ k_- k_+ k_- \right) \\ &\quad + \gamma_D \left(\sigma_- k_+ + \sigma_+ k_- \right) \end{aligned} \tag{22}$$

with renormalized Dresselhaus coefficients β_D and γ_D. The detailed expressions for β_D and γ_D are given in the Appendix. With both Rashba and Dresselhaus terms present the energy dispersion relation becomes

$$E(k) = Ak^2 - Bk^4 \pm \sqrt{(|\alpha_R|^2 + \beta_D^2)k^6 + 2\beta_D\gamma_D k^4 + \gamma_D^2 k^2 + 2|\alpha_R|(k^2\beta_D + \gamma_D)k^4 \sin 2\phi} \tag{23}$$

where $\phi = \arctan(k_y/k_x)$.

We find that, for the single heterojunctions studied here, the magnitudes of the Dresselhaus coefficients are always smaller than the Rashba counterpart (see Appendix). Nevertheless, the term proportional to $\sin 2\phi$ causes the difference $\Delta k_F \equiv |k_{F+} - k_{F-}|$ to be anisotropic in $\boldsymbol{k}$. In accordance to Eq. (22), Δk_F is largest when $\phi = \frac{\pi}{4}$ and smallest when $\phi = \frac{3\pi}{4}$. The anisotropy of the spin splitting, which we define here as the ratio $\kappa \equiv \Delta k_F(\phi = \frac{\pi}{4})/\Delta k_F(\phi = \frac{3\pi}{4})$, depends on the density as well as the material, as Fig. 8 shows. For example, one can infer from Fig. 8(a) that $\kappa = 2.53$ for a GaAs inversion layer with $p = 5 \times 10^{14}$ m^{-2} and $\kappa = 1.86$ with $p = 3 \times 10^{15}$ m^{-2}. The fact that the anisotropy κ decreases with density suggests that the Rashba coefficient increases faster with density than the cubic and linear Dresselhaus coefficients combined (see Appendix). Comparing different materials [Fig. 8(b)], one can deduce that $\kappa = 2.03$, $\kappa = 1.42$, $\kappa = 1.66$ for GaAs, InAs, and InSb inversion layers with $p = 1 \times 10^{15}$ m^{-2}, respectively. This implies that, amongst the materials considered here, the effect of Dresselhaus SOI is weakest in InAs but strongest in GaAs.

TABLE III. Values for material-dependent constants A (in 10^{-16} meV m^2), B (in 10^{-32} meV m^4), and C (in 10^{-24} meV m^3) in the dispersion relation $E(k) = Ak^2 - Bk^4 \pm Ck^3$ for GaAs, InAs, and Ge inversion layers with $N_D - N_A = 3 \times 10^{20}$ m^{-3}. The Schrieffer-Wolff approach breaks down for densities $> 0.5 \times 10^{15}$ m^{-2} for InAs and $> 0.5 \times 10^{15}$ m^{-2} for Ge. All densities below are in 10^{15} m^{-2}.

	GaAs			InAs			Ge		
Density	A	B	C	A	B	C	A	B	C
0.5	3.02	0.28	0.51	9.21	2.09	3.54	5.93	1.18	1.53
1.0	3.00	0.27	0.53						
1.5	2.98	0.25	0.56						
2.0	2.96	0.24	0.58						
2.5	2.94	0.24	0.61						
3.0									

TABLE IV. The energy spacing (in meV) between the HH1 and LH1 level as well as the Fermi energy for GaAs, InAs, and Ge holes inversion layers at various densities (in 10^{15} m^{-2}) and $N_D - N_A = 3 \times 10^{20}$ m^{-3}. The values listed below suggest that LH1 is far away, thus validating the assumption that only the HH1 band is occupied.

	GaAs			InAs			Ge		
Density	E_{H1}	Δ_{11}^{HL}	E_{F1}	E_{H1}	Δ_{11}^{HL}	E_{F1}	E_{H1}	Δ_{11}^{HL}	E_{F1}
0.5	16.12	8.32	0.91	12.87	10.87	2.27	14.72	7.74	1.63
1.0	19.24	8.73	1.67	16.38	11.42	3.47	18.04	8.16	2.72
1.5	22.12	9.04	2.30	19.54	11.79	4.33	21.08	8.46	3.50
2.0	24.83	9.27	2.83	22.47	12.06	5.12	23.91	8.69	4.18
2.5	27.40	9.46	3.26	25.21	12.28	5.88	26.58	8.87	4.80
3.0	29.85	9.62	3.64	27.82	12.45	6.61	29.13	9.02	5.43

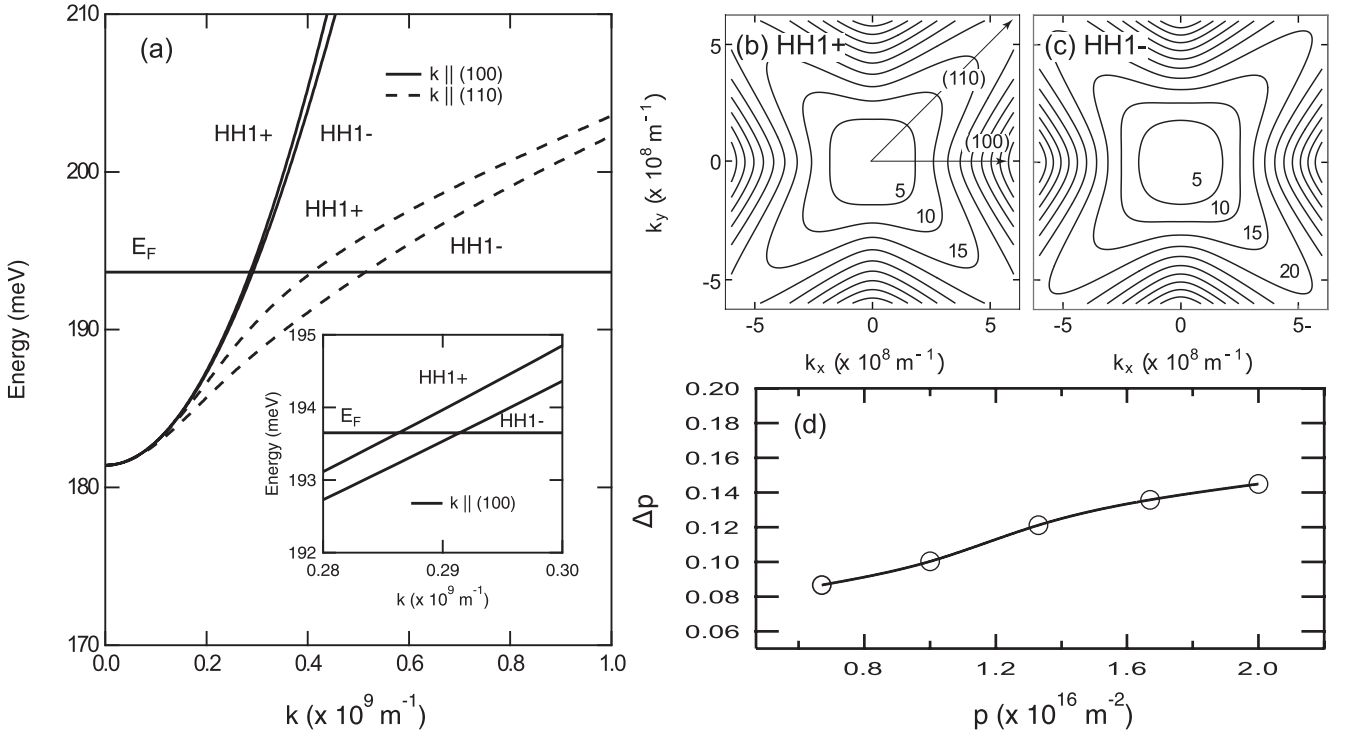

FIG. 7. Panel (a) shows the dispersion for Si holes along (100) and (110), indicating that the strength of spin-orbit interaction is maximum along (110) but minimum along (100). The inset shows that the spin splitting is only 6×10^6 m^{-1} along (100), compared to 1×10^8 m^{-1} along (110). Here, the density is 2×10^{16} m^{-2} and the doping concentration is $N_D - N_A = 3 \times 10^{23}$ m^{-3}. The equienergy contours (separated by 5 meV) for the (b) HH1+ and (c) HH1− subbands in the inversion layer discussed in panel (a) show a severe valence band warping. Panel (d) shows the spin splitting for Si hole inversion layers at various densities with $N_D - N_A = 3 \times 10^{23}$ m^{-3}.

TABLE V. The energy spacing (in meV) between the HH1 and LH1 level as well as the Fermi energy E_{F1} for InSb holes inversion layer with $N_D - N_A = 3\times10^{20}$ m^{-3}. At the densities below (in 10^{15} m^{-2}), only the HH1+ and HH1− bands are occupied.

Density	E_{H1}	InSb Δ_{11}^{HL}	E_{F1}
0.50	10.87	12.00	2.87
0.67	12.02	12.23	3.33
0.83	13.05	12.42	3.74
1.00	14.11	12.59	4.15

TABLE VI. Si holes inversion layer energy level spacings (in meV) for various densities (in 10^{16} m^{-2}), showing that only the HH1+ and HH1− bands are occupied. The dopant concentration $N_D - N_A$ for the inversion layer is 3×10^{23} m^{-3}.

Density	E_{H1}	Si Δ_{11}^{HL}	E_{F1}
0.83	152.81	15.36	6.62
1.00	157.13	15.51	7.64
1.33	165.36	15.75	9.36
1.67	173.63	15.96	10.87
2.00	181.48	16.12	12.17

V. DISCUSSION

The analysis presented in this work is consistent with the known general trend that SO coupling in 2DHGs increases with density. We have characterized the strength of the Rashba SO interaction using both the relative spin-split population difference Δp and the effective masses $m_\pm$. We have found that Δp and m_+ are expected to increase almost linearly with density whereas m_- is approximately constant. While the simple dispersion found using the SW provides a good approximation for certain systems, e.g. GaAs inversion layers with $N_D - N_A = 3 \times 10^{20}$ m^{-3} with densities $p < 2.5 \times 10^{15}$ m^{-2}, there are many parameter regimes in which SW breaks down altogether. The fact that the simple dispersion can break down for realistic parameters challenges the current theories on electric dipole spin resonance (EDSR),[53] spin conductivity,[45–47,50] hole spin helix,[48] and *Zitterbewegung*,[49] which assume that hole spin-orbit coupling is simply cubic in wave vector.

Comparing GaAs inversion and accumulation layers, the strength of the Rashba SO interaction is very sensitive to the type of background dopant. Due to the differing shape of the confinement potentials, the SO interaction is stronger in an accumulation layer than in an inversion layer. In both inversion and accumulation layers, the spin splitting Δp increase with density, yet the dependence of the spin splitting and effective mass on density is quite different. In an accumulation layer, both Δp and m_+ increase almost linearly with density. However, in an accumulation layer, Δp and m_+ saturate at higher densities. These trends can be attributed to the fact that in an accumulation layer, the HH1-LH1 anti-crossing occurs at a lower k, so that the spin splitting near the anti-crossing is reduced. Correspondingly, in accumulation layers SW breaks down at much lower

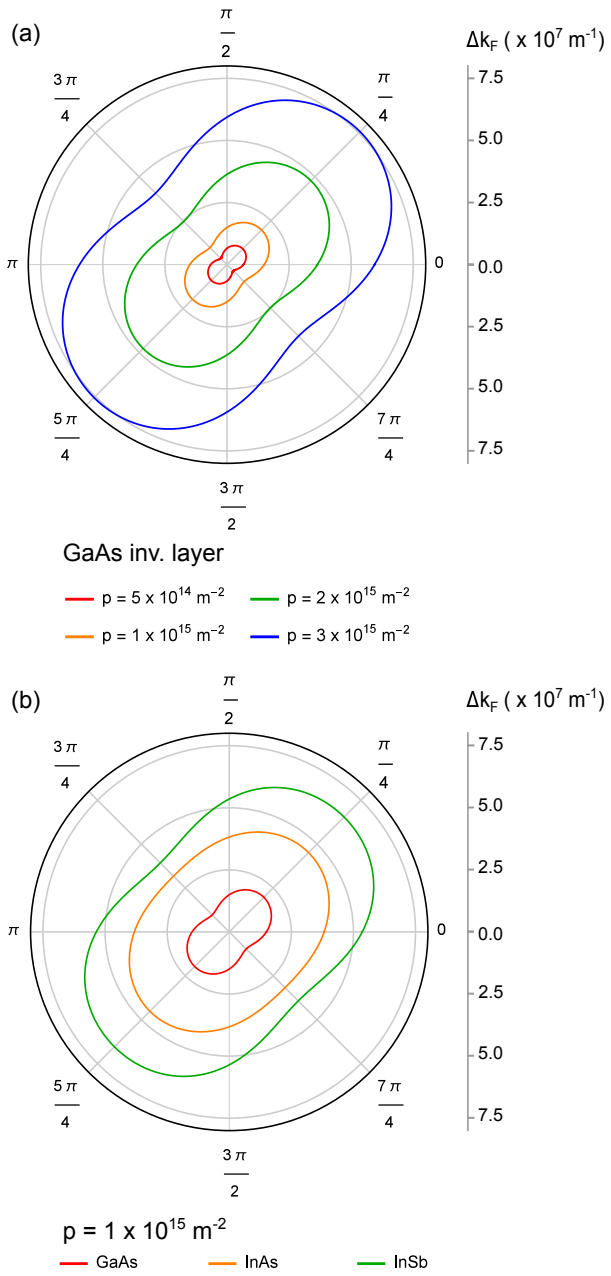

FIG. 8. (Color online) Polar plot of spin splitting $\Delta k_F \equiv |k_{F+} - k_{F-}|$, which is anisotropic in $\boldsymbol{k}$, for (a) GaAs inversion layers at various densities and (b) GaAs, InAs, InSb inversion layers at $p = 1 \times 10^{15}$ m^{-2} in the presence of both Rashba and Dresselhaus interactions. Here, the dopant concentration is $N_D - N_A = 3 \times 10^{20}$ m^{-3}. The angle ϕ is defined as $\phi = \arctan(k_y/k_x)$.

densities than in inversion layers.

We compare our results for GaAs, InAs, InSb, Ge and Si inversion layers. The spin splitting and effective mass profiles show that the Rashba SO interaction is stronger in Ge, InAs, and InSb than in GaAs, though the Fermi contour remains isotropic in the absence of Dresselhaus terms. The Si dispersion, on the other hand, is very anisotropic owing to the large cubic contribution stemming from the bulk Luttinger Hamiltonian.[6] The δ term in the Luttinger Hamiltonian (1) is not negligible and is responsible for the highly anisotropic Fermi contour. The spin splitting is maximum along the (110) and $(1\bar{1}0)$ directions but minimum along (100) and (010).

We have considered the Dresselhaus spin-orbit interaction in zincblende semiconductors GaAs, InAs, and InSb. While the magnitude of BIA is always much smaller than SIA, it causes the spin splitting to be anisotropic in $\boldsymbol{k}$. Fig. 8 shows that the spin splitting is maximum along (110) but minimum along $(1\bar{1}0)$, in accordance with Eq. (23).

VI. SUMMARY

We have performed a variational analysis of spin-orbit interactions in 2D hole gases in inversion-asymmetric wells in a number of cubic semiconductors. We have quantified our findings in terms of experimentally-accessible quantities: carrier number density, effective masses, spin splitting. We find that for a broad range of experimentally relevant parameters the simple Schrieffer-Wolff approximation frequently used to model low dimensional hole structures breaks down. To address this shortcoming we have provided a simple quasi-analytical scheme for calculating spin-orbit related quantities that is in good agreement with numerical studies and experimental data. We recover the known general trend that the spin splitting and HH1+ effective mass m_+ increase as functions of density. We have found that the strength of Rashba SO coupling is much stronger in accumulation layers than in inversion layers, and it is in general much stronger than the Dresselhaus SO coupling, and is very sensitive to the type and density of background dopants. Finally, in Si, due to the strong cubic terms already present in the bulk, the Fermi contour is strongly anisotropic.

ACKNOWLEDGEMENTS

This work has been supported by the ARC through the DP scheme. RW was supported by the NSF under grant No. DMR-1310199. Work at Argonne was supported by DOE BES under Contract No. DE-AC02-06CH11357. We thank Ulrich Zuelicke, Oleg Sushkov, Tommy Li, and Dima Miserev for insightful comments and discussions. We are also indebted to Scott Liles and Ashwin Srinivasan for providing their experimental data for comparison.

Appendix: The material- and structure-dependent parameters

Using the Schrieffer-Wolff transformation, the heavy hole dispersion relation can be written as $E(k) = Ak^2 - Bk^4 \pm Ck^3$. In this section we list the main contributions to A, B, and C. When only the Rashba spin-orbit interaction is considered, $C \equiv |\alpha_R|$. When the Dresselhaus spin-orbit interaction is also included, Ck^3 is replaced by the third term in Eq. (23).

1. First-order terms

The first-order term in the perturbation expansion is given by the diagonal elements in the 2×2 submatrix spanned by the states $|\pm\frac{3}{2}\rangle$ in the Luttinger Hamiltonian (10), i.e.,

$$A^{(1)} = \frac{\mu}{2}(\gamma_1 + \gamma_2). \tag{A.1}$$

Similarly, the linear-k Dresselhaus term gives

$$\gamma_D^{(1)} = -\frac{\sqrt{3}}{2} C_D. \tag{A.2}$$

2. Second-order terms

In this section, we list the second-order terms in Eqs. (A.3)–(A.10) as well as their typical magnitudes (Table VII) for GaAs inversion layers with hole densities of 5×10^{14} m^{-2} and 2×10^{15} m^{-2}.

The expressions for the second-order terms $A^{(2)}$ and $B^{(2)}$ are:

$$A^{(2)} = -3\mu^2 \gamma_3^2 \left(\frac{|\langle H_1|k_z|L_1\rangle|^2}{\Delta_{11}^{HL}} + \frac{|\langle H_1|k_z|L_2\rangle|^2}{\Delta_{12}^{HL}} \right) \tag{A.3}$$

$$B^{(2)} = -\frac{3}{16}\mu^2(\gamma_2 + \gamma_3)^2 \left(\frac{|\langle H_1|L_1\rangle|^2}{\Delta_{11}^{HL}} + \frac{|\langle H_1|L_2\rangle|^2}{\Delta_{12}^{HL}} \right) \tag{A.4}$$

where $\Delta_{pq}^{rs} \equiv |E_p^r - E_q^s|$. Typical values for $A^{(2)}$ and $B^{(2)}$ for GaAs inversion layers are given in Table VII.

The Rashba and Dresselhaus terms, on the other hand, are obtained from the off-diagonal elements of the 2×2 matrix. The presence of these terms lift the spin-degeneracy. The expressions for Rashba and Dresselhaus terms are given in the Eqs. (A.5)–(A.10).

TABLE VII. Typical values for A (in 10^{-16} meV m^2), B (in 10^{-32} meV m^4), $|\alpha_R|$, β_D (both in 10^{-24} meV m^3), and γ_D (in 10^{-8} meV m) for 2DHG GaAs hole inversion layers with $N_D - N_A = 3 \times 10^{20}$ m^{-3}. The density is in 10^{15} m^{-2}. Note that here the Dresselhaus coefficients are always smaller than the Rashba coefficient.

density	$A^{(1)}$	$A^{(2)}$	$B^{(2)}$	$\lvert\alpha_R^{(2)}\rvert$	$\beta_D^{(2)}$	$\gamma_D^{(1)}$	$\gamma_D^{(2)}$
0.5	3.42	−0.42	−0.28	0.53	0.080	0.029	0.008
2.0	3.42	−0.61	−0.22	0.65	0.084	0.029	0.011

The second-order Rashba term $\alpha_R^{(2)}$ reads

$$\alpha_R^{(2)} = -\frac{3}{4}\mu^2\gamma_3(\gamma_2+\gamma_3)\left(\frac{\langle L_1|k_z|H_1\rangle\langle H_1|L_1\rangle - \langle H_1|k_z|L_1\rangle\langle L_1|H_1\rangle}{\Delta_{11}^{HL}} + \frac{\langle L_2|k_z|H_1\rangle\langle H_1|L_2\rangle - \langle H_1|k_z|L_2\rangle\langle L_2|H_1\rangle}{\Delta_{12}^{HL}}\right), \tag{A.5}$$

whereas, the second-order cubic Dresselhaus term $\beta_D^{(2)}$ is given as

$$\beta_D^{(2)} = -\frac{\mu}{8}(\gamma_2+\gamma_3)\left[3B_D\left(\frac{\langle L_1|k_z^2|H_1\rangle\langle H_1|L_1\rangle + \langle H_1|k_z^2|L_1\rangle\langle L_1|H_1\rangle}{\Delta_{11}^{HL}} + \frac{\langle L_2|k_z^2|H_1\rangle\langle H_1|L_2\rangle + \langle H_1|k_z^2|L_2\rangle\langle L_2|H_1\rangle}{\Delta_{12}^{HL}}\right)\right] \tag{A.6}$$

Evaluating the expectation values in Eq. (A.5) using the zero- (4) and one-node (9) wave functions, we have

$$\alpha_R^{(2)} = -48i\mu^2\,\gamma_3(\gamma_2+\gamma_3)\lambda_h^3\,(\lambda_h-\lambda_l)\left[\frac{\lambda_l^3}{(\lambda_h+\lambda_l)^6}\frac{1}{\Delta_{11}^{HL}} - \lambda_L^5 \times \frac{-3\lambda_h^2+\lambda_L(-2\lambda_l+\lambda_L)+4\lambda_h(\lambda_l+\lambda_L)}{(\lambda_h+\lambda_L)^8(\lambda_l^2-\lambda_l\lambda_L+\lambda_L^2)}\frac{1}{\Delta_{12}^{HL}}\right]. \tag{A.7}$$

On the other hand, evaluating the expectation values in Eq. (A.6) yields

$$\beta_D^{(2)} = -48\mu\,B_D(\gamma_2+\gamma_3)\lambda_h^4\left[\frac{\lambda_l^4}{(\lambda_h+\lambda_l)^6}\frac{1}{\Delta_{11}^{HL}} - (\lambda_h-\lambda_l)\lambda_L^5 \times \frac{[\lambda_L(-2\lambda_l+\lambda_L)+\lambda_h(\lambda_l+4\lambda_L)]}{(\lambda_h+\lambda_L)^8(\lambda_l^2-\lambda_l\lambda_L+\lambda_L^2)}\frac{1}{\Delta_{12}^{HL}}\right], \tag{A.8}$$

whereas linear-k Dresselhaus coeffcient has the form:

$$\gamma_D^{(2)} = -2\sqrt{3}\mu\,\gamma_3 C_D\left(\frac{|\langle H_1|k_z|L_1\rangle|^2}{\Delta_{11}^{HL}} + \frac{|\langle H_1|k_z|L_2\rangle|^2}{\Delta_{12}^{HL}}\right), \tag{A.9}$$

which, in terms of the variational parameters, equals to

$$\gamma_D^{(2)} = -\frac{32}{\sqrt{3}}\mu\,C_D\gamma_3\lambda_h^3\left[\frac{3\lambda_l^3\,(\lambda_h-\lambda_l)^2}{(\lambda_h+\lambda_l)^6}\frac{1}{\Delta_{11}^{HL}} + \lambda_L^5 \times \frac{\left[-3\lambda_h^2+\lambda_L(-2\lambda_l+\lambda_L)+4\lambda_h(\lambda_l+\lambda_L)\right]^2}{(\lambda_h+\lambda_L)^8(\lambda_l^2-\lambda_l\lambda_L+\lambda_L^2)}\frac{1}{\Delta_{12}^{HL}}\right]. \tag{A.10}$$

The typical magnitudes for the Rashba and Dresselhaus coefficients in the second-order are given in the Table VII. Note that for the Fermi wave vectors considered here the linear Dresselhaus term is comparable in magnitude to the cubic Dresselhaus term.

[1] S. Datta and B. Das, Appl. Phys. Lett. **56**, 665 (1990).
[2] I. Žutić, J. Fabian, and S. Das Sarma, Rev. Mod. Phys. **76**, 323 (2004).
[3] D. Loss and D. P. DiVincenzo, Phys. Rev. A **57**, 120 (1998).
[4] D. V. Bulaev and D. Loss, Phys. Rev. Lett. **95**, 076805 (2005).
[5] D. D. Awschalom, L. C. Bassett, S. D. Dzurak, E. L. Hu, and J. R. Petta, Science **339**, 1174 (2013).
[6] R. Winkler, *Spin-Orbit Coupling Effects in Two-Dimensional Electron and Hole Systems* (Springer, Berlin, 2003).

[7] R. Winkler, S. J. Papadakis, E. P. De Poortere, and M. Shayegan, Phys. Rev. Lett. **85**, 4574 (2000).
[8] S. J. Papadakis, E. P. De Poortere, M. Shayegan, and R. Winkler, Phys. Rev. Lett. **84**, 5592 (2000).
[9] H. A. Fertig, Science **301**, 1335 (2003).
[10] L. P. Rokhinson, V. Larkina, Y. B. Lyanda-Geller, L. N. Pfeiffer, and K. W. West, Phys. Rev. Lett. (2004).
[11] J. C. H. Chen, O. Klochan, A. P. Micolich, A. R. Hamilton, T. P. Martin, L. H. Ho, U. Zülicke, D. Reuter, and A. D. Wieck, New J. Phys. **12**, 033043 (2010).
[12] O. Klochan, J. C. H. Chen, A. P. Micolich, A. R. Hamilton, K. Muraki, and Y. Hirayama, Appl. Phys. Lett. **96**, 092103 (2010).
[13] Z. K. Keane, M. C. Godfrey, J. C. H. Chen, S. Fricke, O. Klochan, A. M. Burke, A. P. Micolich, H. E. Beere, D. A. Ritchie, K. V. Trunov, D. Reuter, A. D. Wieck, and A. R. Hamilton, Nano Lett. **11**, 3147 (2011).
[14] Y. Komijani, M. Csontos, I. Shorubalko, U. Zülicke, T. Ihn, K. Ensslin, D. Reuter, and A. D. Wieck, Europhys. Lett. **102**, 37002 (2013).
[15] R. Li, F. E. Hudson, A. S. Dzurak, and A. R. Hamilton, Appl. Phys. Lett. **103**, 163508 (2013).
[16] P. C. Spruijtenburg, J. Ridderbos, F. Mueller, A. W. Leenstra, M. Brauns, A. A. I. Aarnink, W. G. Van Der Wiel, and F. A. Zwanenburg, Appl. Phys. Lett. **102**, 192105 (2013).
[17] A. Srinivasan, L. A. Yeoh, O. Klochan, T. P. Martin, J. C. H. Chen, A. P. Micolich, A. R. Hamilton, D. Reuter, and A. D. Wieck, Nano Lett. **13**, 148 (2013).
[18] F. Nichele, S. Chesi, S. Hennel, A. Wittmann, C. Gerl, W. Wegscheider, D. Loss, T. Ihn, and K. Ensslin, Phys. Rev. Lett. **113**, 046801 (2014).
[19] L. A. Tracy, T. W. Hargett, and J. L. Reno, Appl. Phys. Lett. **104**, 123101 (2014).
[20] R. Li, F. E. Hudson, A. S. Dzurak, and A. R. Hamilton, Nano Lett. **15**, 7314 (2015).
[21] F. Mueller, G. Konstantaras, P. C. Spruijtenburg, W. G. van der Wiel, and F. A. Zwanenburg, Nano Lett. **15**, 5336 (2015).
[22] M. Brauns, J. Ridderbos, A. Li, E. P. A. M. Bakkers, and F. A. Zwanenburg, Phys. Rev. B **93**, 121408(R) (2016).
[23] P. Yu and M. Cardona, *Fundamentals of Semiconductors: Physics and Materials Properties*, 3rd ed. (Springer, Berlin, 1996).
[24] J. M. Luttinger, Phys. Rev. **102**, 1030 (1956).
[25] D. Culcer, C. Lechner, and R. Winkler, Phys. Rev. Lett. **97**, 106601 (2006).
[26] D. Culcer and R. Winkler, Phys. Rev. B **76**, 195204 (2007).
[27] R. Winkler, D. Culcer, S. J. Papadakis, B. Habib, and M. Shayegan, Semicond. Sci. Tech. **23**, 114017 (2008).
[28] Y. A. Bychkov and E. I. Rashba, J Phys. C: Solid State **17**, 6039 (1984).
[29] G. Dresselhaus, Phys. Rev. **100**, 580 (1955).
[30] D. A. Broido and L. J. Sham, Phys. Rev. B **31**, 888 (1985).
[31] U. Ekenberg and M. Altarelli, Phys. Rev. B **30**, 3569 (1984).
[32] S. Mori and T. Ando, Phys. Rev. B **19**, 6433 (1979).
[33] O. V. Volkov, Phys. Solid State **40**, 1019 (1998).
[34] G. Goldoni and M. Peeters, Phys. Rev. B **51**, 17806 (1995).
[35] E. Bangert and G. Landwehr, Superlatt. Microstruct. **7**, 363 (1985).
[36] R. Winkler, H. Noh, E. Tutuc, and M. Shayegan, Phys. Rev. B **65**, 155303 (2002).
[37] A. Manaselyan and T. Chakraborty, Europhys. Lett. **88**, 17003 (2009).
[38] J. M. Luttinger and W. Kohn, Phys. Rev. **97**, 869 (1954).
[39] F. F. Fang and W. E. Howard, Phys. Rev. Lett. **16**, 797 (1966).
[40] M. J. Kelly and A. Hamilton, Semicond. Sci. Tech. **6**, 201 (1991).
[41] R. Winkler, U. Kunze, and U. Rössler, Surf. Sci. **263**, 222 (1992).
[42] J. R. Schrieffer and P. A. Wolff, Phys. Rev. **149**, 491 (1966).
[43] P.-O. Löwdin, J. Chem. Phys. **19**, 1396 (1951).
[44] M. V. Durnev, M. M. Glazov, and E. L. Ivchenko, Phys. Rev. B **89**, 075430 (2014).
[45] N. Sugimoto, S. Onoda, S. Murakami, and N. Nagaosa, Phys. Rev. B **73**, 113305 (2006).
[46] A. Wong and F. Mireles, Phys. Rev. B **81**, 085304 (2010).
[47] X. Bi, P. He, E. M. Hankiewicz, R. Winkler, G. Vignale, and D. Culcer, Phys. Rev. B **88**, 035316 (2013).
[48] V. E. Sacksteder and B. A. Bernevig, Phys. Rev. B **89**, 161307 (2014).
[49] T. Biswas, S. Chowdhury, and T. K. Ghosh, Eur. Phys. J. B **88**, 220 (2015).
[50] J. Schliemann and D. Loss, Phys. Rev. B **69**, 165315 (2004).
[51] D. Culcer and R. Winkler, Phys. Rev. Lett. **99**, 226601 (2007).
[52] D. Culcer and R. Winkler, Phys. Rev. B **76**, 245322 (2007).
[53] D. V. Bulaev and D. Loss, Phys. Rev. Lett. **98**, 097202 (2007).
[54] R. Winkler, J. Phys. Condens. Matter **5**, 2321 (1993).
[55] E. K. U. Gross, E. Runge, and O. Heinoen, *Many-Particle Theory* (IOP, Bristol, 1991).
[56] T. Ando, A. B. Fowler, and F. Stern, Rev. Mod. Phys. **54**, 437 (1982).
[57] T. Ando, J. Phys. Soc. Jpn. **51**, 3893 (1982).
[58] F. Nichele, A. N. Pal, R. Winkler, C. Gerl, W. Wegscheider, T. Ihn, and K. Ensslin, Phys. Rev. B **89**, 1 (2014).
[59] B. Grbic, *Hole transport and spin-orbit coupling in p-type GaAs nanostructures*, Ph.D. thesis, ETH Zurich (2007).
[60] S. Liles and A. Srinivasan, (2016), unpublished.
[61] H. L. Störmer, Z. Schlesinger, A. Chang, D. C. Tsui, A. C. Gossard, and W. Wiegmann, Phys. Rev. Lett. **51**, 126 (1983).
[62] M. V. Fischetti, Z. Ren, P. M. Solomon, M. Yang, and K. Rim, J. Appl. Phys. **94**, 1079 (2003).